

# Central Mass Profiles of the Nearby Cool-core Galaxy Clusters Hydra A and A478<sup>\*</sup>

N. Okabe<sup>1,2,3,4†</sup>, K. Umetsu<sup>4</sup>, T. Tamura<sup>5</sup>, Y. Fujita<sup>6</sup>, M. Takizawa<sup>7</sup>,  
K. Matsushita<sup>8</sup>, Y. Fukazawa<sup>2</sup>, T. Futamase<sup>9</sup>, M. Kawaharada<sup>5</sup>,  
S. Miyazaki<sup>10</sup>, Y. Mochizuki<sup>8</sup>, K. Nakazawa<sup>11</sup>, T. Ohashi<sup>12</sup>, N. Ota<sup>13</sup>,  
T. Sasaki<sup>8</sup>, K. Sato<sup>8</sup>, and S. I. Tam<sup>14</sup>

<sup>1</sup> *Department of Physical Science, Hiroshima University, 1-3-1 Kagamiyama, Higashi-Hiroshima, Hiroshima 739-8526, Japan*

<sup>2</sup> *Hiroshima Astrophysical Science Center, Hiroshima University, Higashi-Hiroshima, Kagamiyama 1-3-1, 739-8526, Japan*

<sup>3</sup> *Kavli Institute for the Physics and Mathematics of the Universe (WPI),*

*Todai Institutes for Advanced Study, University of Tokyo, 5-1-5 Kashiwanoha, Kashiwa, Chiba 277-8583, Japan*

<sup>4</sup> *Institute of Astronomy and Astrophysics, Academia Sinica, P.O. Box 23-141, Taipei 10617, Taiwan*

<sup>5</sup> *Institute of Space and Astronautical Science, Japan Aerospace Exploration Agency,*

*3-1-1 Yoshinodai, Chuo-ku, Sagami-hara, Kanagawa 229-8510, Japan*

<sup>6</sup> *Department of Earth and Space Science, Graduate School of Science, Osaka University, Toyonaka, Osaka 560-0043, Japan*

<sup>7</sup> *Department of Physics, Yamagata University, Kojirakawa-machi 1-4-12, Yamagata 990-8560, Japan*

<sup>8</sup> *Department of Physics, Tokyo University of Science, 1-3 Kagurazaka, Shinjyuku-ku, Tokyo 162-8601, Japan*

<sup>9</sup> *Astronomical Institute, Tohoku University, Aramaki, Aoba-ku, Sendai 980-8578, Japan*

<sup>10</sup> *National Astronomical Observatory of Japan, Mitaka, Tokyo 181-8588, Japan*

<sup>11</sup> *Department of Physics, The University of Tokyo, 7-3-1 Hongo, Bunkyo-ku, Tokyo 113-0033, Japan*

<sup>12</sup> *Department of Physics, Tokyo Metropolitan University, 1-1 Minami-Osawa, Hachioji, Tokyo 192-0397, Japan*

<sup>13</sup> *Department of Physics, Nara Women's University, Kita-uoyanishi-machi, Nara, Nara 630-8506, Japan*

<sup>14</sup> *Department of Physics, National Taiwan University, Taipei 10617, Taiwan*

14 December 2015

## ABSTRACT

We perform a weak-lensing study of the nearby cool-core galaxy clusters, Hydra A ( $z = 0.0538$ ) and A478 ( $z = 0.0881$ ), of which brightest cluster galaxies (BCGs) host powerful activities of active galactic nuclei (AGNs). For each cluster, the observed tangential shear profile is well described either by a single Navarro–Frenk–White model or a two-component model including the BCG as an unresolved point mass. For A478, we determine the BCG and its host-halo masses from a joint fit to weak-lensing and stellar photometry measurements. We find that the choice of initial mass functions (IMFs) can introduce a factor of two uncertainty in the BCG mass, whereas the BCG host halo mass is well constrained by data. We perform a joint analysis of weak-lensing and stellar kinematics data available for the Hydra A cluster, which allows us to constrain the central mass profile without assuming specific IMFs. We find that the central mass profile ( $r < 300$  kpc) determined from the joint analysis is in excellent agreement with those from independent measurements, including dynamical masses estimated from the cold gas disk component, X-ray hydrostatic total mass estimates, and the central stellar mass estimated based on the Salpeter IMF. The observed dark-matter fraction around the BCG for Hydra A is found to be smaller than those predicted by adiabatic contraction models, suggesting the importance of other physical processes, such as the AGN feedback and/or dissipationless mergers.

**Key words:** galaxies: clusters: individual (Hydra A, A478) - gravitational lensing: weak

<sup>\*</sup> Based on data collected at Subaru Telescope, which is operated by the National Astronomical Observatory of Japan.

<sup>†</sup> E-mail: okabe@hiroshima-u.ac.jp

## 1 INTRODUCTION

The standard cold-dark-matter (CDM) paradigm excellently describes the statistical properties and growth of cosmic structure from the early universe to the present day epoch, as observed from the cosmic microwave background radiation (e.g. Hinshaw et al. 2013; Planck Collaboration et al. 2013) and large scale clustering of galaxies (e.g. Percival et al. 2001; Anderson et al. 2014). Cosmological simulations of collisionless CDM predict that the quasi-equilibrium mass density profile of dark-matter halos formed by collisionless gravitational dynamics is nearly universal and self-similar over wide mass ranges (Navarro, Frenk & White 1996, hereafter NFW). The spherically-averaged density profile exhibits a soft cusp ( $\rho \propto r^{-1}$ ) in the center and has steeper slopes at larger halo radii ( $\rho \propto r^{-3}$  in the outskirts). Recent observations of stacked weak gravitational lensing signals for massive galaxy clusters at  $z \sim 0.2$  (Oguri et al. 2012; Okabe et al. 2010, 2013; Okabe & Smith 2015; Umetsu et al. 2011, 2014, 2015b; Niikura et al. 2015) revealed that the observed cluster lensing profiles are in excellent agreements with the NFW density profile predicted for collisionless CDM halos. However, since the innermost cluster radius for weak lensing is typically limited to  $r \sim 100h^{-1}$  kpc due to the finite resolution of weak-lensing observations, it is practically difficult to directly constrain the innermost cluster mass distribution around bright cluster galaxies (BCGs).

The total mass density profiles of clusters in the central region have been a subject of intense theoretical and observational studies. Numerical simulations of collisionless dark matter show that the central cusp slope of dark-matter halos is not strictly self similar (Gao et al. 2012). Baryonic effects cannot be ignored in the central region where the cooling time is shorter than the Hubble time and rich stellar populations within BCGs are abundant. Stars form from radiative gas cooling, and subsequently dark matter is pulled inward in response to the central condensation of baryons. A cuspy dark-matter density profile is formed through such energy exchange processes between dark matter and baryons, which is referred to as *adiabatic contraction* (e.g. Eggen, Lynden-Bell & Sandage 1962; Blumenthal et al. 1986; Gao et al. 2004; Gnedin et al. 2004). On the other hand, if BCGs are formed by the accretion of clumpy structures such as satellite galaxies and globular clusters, a cored density profile is expected to form by dynamical friction (e.g. El-Zant, Shlosman & Hoffman 2001; Lackner & Ostriker 2010). Gas outflows driven by active galactic nuclei (AGNs) can suppress condensation of gas and stars, resulting in flattening of the dark-matter distribution in the central region (e.g. Teyssier et al. 2011; Martizzi et al. 2012; Ragone-Figueroa, Granato & Abadi 2012).

Stellar kinematics of BCGs is one of the most powerful means of measuring the total mass profile in the central region of galaxies (e.g. Cappellari et al. 2006). Recently, Newman et al. (2009, 2011, 2013) measured the total mass profiles of relaxed clusters and decomposed them into stellar and dark-matter components from joint measurements of strong/weak lensing and stellar kinematics within BCGs, under the assumptions of dynamical equilibrium, isotropic orbits, and constant stellar mass-to-light ratio. Oguri, Rusu & Falco (2014) carried out a joint ensemble

analysis of strong lensing and stellar photometry data for a large sample of 161 elliptical galaxies to measure their average mass density profile. Stellar mass estimates for galaxies can be obtained from stellar photometry using scaling relations between galaxy luminosity and stellar mass, whereas the stellar initial mass function (IMF) governs the normalization of the stellar mass to luminosity relation. Hence, the uncertainty of the stellar IMF can give rise to a systematic bias in stellar mass estimates. In order to break the degeneracy between the IMF uncertainty and the inner slope of the mass density profile, Oguri, Rusu & Falco (2014) proposed to use quasar microlensing observations.

We have two ideal clusters, Hydra A ( $z = 0.0538$ ; Sato et al. 2012) and Abell 478 ( $z = 0.0881$ ; Mochizuki et al. 2014), to study the mass distributions within both clusters and BCGs. The two clusters have been selected and observed as targets of joint Subaru weak-lensing and *Suzaku* X-ray studies (Okabe et al. 2014b). They are well-known cool-core clusters hosting central AGNs inside their BCGs. Recent X-ray and radio observations (e.g. McNamara et al. 2000; David et al. 2001; Wise et al. 2007; Sun et al. 2003; Sanderson, Finoguenov & Mohr 2005; Diehl et al. 2008) have shown that giant radio lobes triggered by prominent AGN jets are interacting with the surrounding intracluster medium (ICM). Isobaric cooling time scales in the central region are shorter than 1 Gyr. Hence, the clusters provide us with unique environments for studying the effects of baryons acting on the dark-matter distribution in the cluster center.

Since these clusters are at very low redshifts, their large angular extents enable us to detect weak-lensing signals around the BCGs, in particular for Hydra A, and to measure the radial mass distribution, by using the unique combination of weak lensing and stellar kinematics or stellar photometry. For these very nearby clusters, especially for the Hydra A cluster, strong-lensing information is not needed to resolve the central matter distribution.

This paper is organized as follows. In Section 2, we conduct shape measurements, examine the redshift dependence of the contamination level by member galaxies, and securely select background galaxies. We measure cluster masses in Section 3, perform joint analyses in Section 4, and discuss the results in Section 5. Section 6 is devoted to the summary. A comparison of weak-lensing masses and *Suzaku* X-ray observables is given in our previous paper (Okabe et al. 2014b). We use  $\Omega_{m,0} = 0.27$ ,  $\Omega_{\Lambda} = 0.73$  and  $H_0 = 70h_{70}$  km s $^{-1}$  Mpc $^{-1}$ .

## 2 DATA ANALYSIS

### 2.1 Data Analysis and Shape Measurement

We conducted observations of Hydra A and Abell 478 using the Subaru/Suprime-cam (Miyazaki et al. 2002), in  $i'$  and  $g'$  bands, on Jan 7th, 2013. The  $i'$  imaging was taken to measure ellipticities of galaxies for the weak-lensing shape analysis. The two-band photometry in the  $g'$  and  $i'$  bands is to minimize contamination of the background source catalog by unlensed cluster member galaxies. The Hydra A and Abell 478 fields are covered by a mosaic of 8 and 9 pointings, respectively, as shown in Figure 1. We note that, for

**Table 1.** Summary of Subaru observations for Hydra A and Abell 478. Each pointing is shown in Figure 1. The seeing FWHM is for the  $i'$ -band used for shape measurements.

Name	$i'$ [min]	$g'$ [min]	Seeing [arcsec]
HYDRAA_00	15.0	11.7	0.75
HYDRAA_02	15.0	10.0	0.71
HYDRAA_10	15.0	11.7	0.73
HYDRAA_11	15.0	11.2	0.71
HYDRAA_12	15.0	10.0	0.63
HYDRAA_20	15.0	11.7	0.67
HYDRAA_21	15.0	11.2	0.71
HYDRAA_22	15.0	10.0	0.65
ABELL478_00	15.0	11.7	0.67
ABELL478_01	15.0	11.7	0.79
ABELL478_02	15.0	11.7	0.73
ABELL478_10	15.0	11.7	0.65
ABELL478_11	15.0	11.7	0.79
ABELL478_12	15.0	11.7	0.71
ABELL478_20	15.0	14.0	0.69
ABELL478_21	15.0	11.7	0.69
ABELL478_22	15.0	11.7	0.71

Hydra A, the middle-east pointing was not available as limited by the number of allocated nights and bright stars in that region. The observing conditions are summarized in Table 1. The typical seeing is  $\sim 0.7''$  in the  $i'$  band for weak-lensing shape measurements. The exposure times for the  $i'$  and  $g'$  bands are  $\sim 15$  and  $\sim 12$  min, respectively. These are about half of those typically used in our previous weak-lensing studies of intermediate-redshift clusters at  $z \sim 0.2$  (e.g., Okabe & Umetsu 2008; Okabe et al. 2010, 2013; Okabe & Smith 2015). We used the standard Suprime-Cam reduction software SDFRED (Yagi et al. 2002; Ouchi et al. 2004) modified to accommodate new CCD chips, for flat-fielding, instrumental distortion correction, differential refraction, point-spread-function (PSF) matching, sky subtraction and stacking. An astrometric calibration was conducted with 2MASS point sources (Skrutskie et al. 2006). Typical residual astrometric offsets are no larger than the CCD pixel size.

We determine the mass distribution in nearby clusters using weak gravitational lensing. Weak lensing analysis is performed following Kaiser, Squires & Broadhurst (1995) with some modifications (Okabe et al. 2013, 2014a; Okabe & Smith 2015). Technical details are described in Okabe et al. (2014a). The image ellipticity  $e_\alpha$  of an object detected in the  $i'$  band data is measured from weighted quadrupole moments of the surface brightness distribution. The PSF anisotropy is corrected for using second-order bipolynomial functions of the stellar anisotropy kernel, which is expressed with KSB’s smear polarizability tensor and image ellipticity of unsaturated stars. To examine the validity of anisotropic PSF corrections, we have checked residual systematics in corrected ellipticities as described in Appendix of Okabe et al. (2014a). Two-point correlation functions between star and galaxy ellipticities after the correction are of the order of  $10^{-8}$ – $10^{-6}$ , significantly improved from  $10^{-5}$ – $10^{-4}$  before the correction. This level of residual

correlations is consistent with zero. The reduced shear signal is obtained by applying a correction for the isotropic smearing effect as  $g_\alpha = (P_g^{-1})_{\alpha\beta} e'_\beta$ . Here,  $e'_\alpha$  is the image ellipticity after the anisotropic PSF correction and  $P_{\alpha\beta}^g$  is the pre-seeing shear polarizability tensor. Since the measurement of  $P_{\alpha\beta}^g$  is very noisy for faint individual galaxies,  $P_{\alpha\beta}^g$  is calibrated using galaxies detected with high signal-to-noise ratio  $\nu > 30$ , following Okabe et al. (2014a). Similar calibration procedures are developed by Umetsu et al. (2010) and Oguri et al. (2012). Our shear calibration on  $g_\alpha$  results in 2–3% accuracy (Okabe et al. 2014a).

We measure magnitudes of galaxies using SExtractor (Bertin & Arnouts 1996). The SExtractor configuration is optimized for shape measurements of faint galaxies. For each object, we compute a total Kron-like magnitude and an aperture magnitude for color measurements in the AB-magnitude system. To perform color measurements, the  $i'$ -band data are degraded to the PSF of  $g'$ -band data. For aperture photometry, the aperture diameter is set to 1.5 times the worst-seeing FWHM. Finally, we combine SExtractor-based photometry with weak-lensing shape measurements to create a weak-lensing-matched photometry catalog.

## 2.2 Background Selection

It is of prime importance for an accurate mass measurement to securely select background galaxies. Contamination of unlensed member and/or foreground galaxies in the shear catalog leads to a systematic underestimation of cluster lensing mass, referred to as a dilution effect (e.g. Broadhurst et al. 2005; Umetsu & Broadhurst 2008; Umetsu et al. 2010; Okabe et al. 2010, 2011, 2013, 2014a). The dilution effect is increasing as a projected cluster-centric radius is decreasing, because the fraction of member galaxies to background galaxies is increasing. The effect is more dominant for more massive clusters. We select background galaxies in color-magnitude plane, following studies for clusters at  $z \sim 0.2$  or higher redshift (Broadhurst et al. 2005; Okabe et al. 2010, 2013). A majority of unlensed galaxies to dilute lensing signals are faint and small member galaxies around the red sequence and apparent magnitudes  $i' \sim 22$ – $26$  ABmag in the color-magnitude plane. Although the red sequence of bright member galaxies are clearly identified in color-magnitude plane because of a passive evolution, the color distribution for faint galaxies becomes unclear as the apparent magnitude becomes fainter. It is therefore very difficult to discriminate between member and background galaxies in the faint end. We thus investigate the color distribution of member galaxies using lensing signals in order to minimize the contamination. We measure a mean tangential distortion strength in the central region of clusters by changing lower limits of color for the background selection,  $\langle g_+ \rangle(> \Delta C) = \sum_i g_{+,i}(> \Delta C) w_{g,i}(> \Delta C) / \sum_i w_{g,i}(> \Delta C)$ . Here,  $\Delta C = (g' - i') - (g' - i')_{E/S0}$  is as a function of color offset from the red sequence,  $g_{+,i}$  is the tangential component of reduced shear of the  $i$ -th galaxies with respect to the cluster center, given by

$$g_{+,i} = -(g_{1,i} \cos 2\varphi + g_{2,i} \sin 2\varphi),$$

and  $w_{g,i} = 1/(\sigma_{g,i}^2 + \alpha^2)$  is a statistical weight. Here,  $\varphi$  is the position angle between the first coordinate axis on

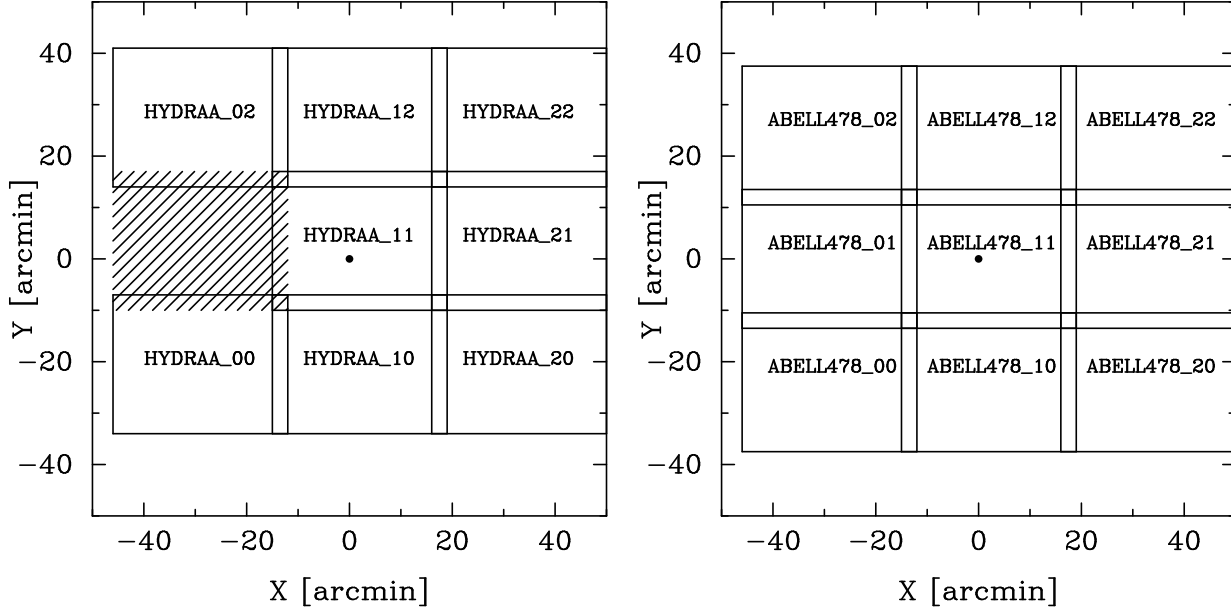


**Figure 1.** Pointing maps for Hydra A (left) and Abell 478 (right). The horizontal and vertical axes are R.A. and Decl. offsets from BCGs, in units of arcmin. For each cluster, the circle represents the position of the BCG:  $(139.524^\circ, -12.095^\circ)$  for Hydra A and  $(63.355^\circ, 10.465^\circ)$  for A478. The pointing IDs (Table 1) are shown for each cluster. The adjacent pointings have an overlap of 2 arcmin. The hatched region indicates that there is no data for the present study.

the sky and the vector connecting the cluster center and the galaxy position. The position of the BCGs is adopted as the cluster center.  $\sigma_{g,i}$  is an rms error of the shear estimate and  $\alpha$  is the softening constant variance representing the scatter due to the intrinsic ellipticity of the galaxies (e.g., Hoekstra, Franx & Kuijken 2000; Hamana et al. 2003; Okabe et al. 2010; Umetsu et al. 2010; Oguri et al. 2012). We choose  $\alpha = 0.4$ .

In order to clarify the dilution effect in noisy lensing signals, the mean distortion strength is cumulatively computed as a function of color offset from the red sequence,  $\Delta C$ . We choose the central region of  $100 - 500 h_{70}^{-1}$  kpc from brightest cluster galaxies (BCGs). We also compute the mean lensing depth  $\langle D_{ls}/D_s \rangle$ . Since it is difficult to estimate photometric redshifts of individual objects using two bands, we used the COSMOS photometric redshift catalog (Ilbert et al. 2009) estimated by combining 30 bands. The mean photometric redshift is computed with a statistical weight of  $w_g$  by matching with the COSMOS photometric redshift in color-magnitude plane. If there were no contamination of unlensed member galaxies, it is expected that a “Dilution” estimator, which is defined by the ratio between the mean lensing signal and depth,  $D = \langle g+ \rangle / \langle D_{ls}/D_s \rangle (> \Delta C)$ , is constant irrespective of the lower limit of the color offset,  $\Delta C$ . Here,  $D_{ls}$  and  $D_s$  are the angular diameter distance between cluster (lens) and source redshifts and between observers and source redshifts, respectively. Therefore,  $D$  is a good estimator to investigate the color distribution of member galaxies.

The resultant  $D$  is shown in the top panel of Figure 2. The red diamonds and blue circles denote  $D$  for A478 and Hydra A, respectively. Although the error is large,  $D$  of A478 is constant at  $\Delta C \sim 0$ , increases with  $\Delta C$  at  $\Delta C \sim 0.1$ , and becomes flat at  $\Delta C > 0.3$ . The small  $D$  at  $\Delta C \sim 0$  indicates a presence of member galaxies. On the other hand,  $D$

of Hydra-A shows a random distribution for  $\Delta C$ , suggesting no significant feature of the contamination. We model a color distribution of  $D$ , given by  $A + B \tanh((\Delta C - \Delta C_0)/\sigma)$ . Here,  $A$  is the normalization at  $\Delta C = 0$ ,  $A + B$  is a mean lensing strength of pure background galaxies, and the second term represents a constant  $D$  at  $\Delta C \sim 0$  and  $\Delta C > 0.3$ . As shown in Figure 2, the best-fit model (red solid line) of A478 well describes the data. As for Hydra A, the best-fit model is consistent with no contamination. We derive a color distribution of contamination level of unlensed galaxies in background shear catalog (the bottom panel of Figure 2). The maximum contamination level is at most 17% at  $\Delta C = 0$ . In order to investigate a cluster-redshift dependence of the dilution effect, we compute the mean  $D$  within the same physical radius for 50 clusters at  $z \sim 0.2$  from the Local Cluster Substructure Survey (LoCuSS). Here,  $\Delta C$  is the color offset from the red sequence in the  $i' - V$  band. The calculation and model for stacked 50 clusters are described in Okabe et al. (2013). The maximum contamination level for 50 clusters (green dashed line in the bottom panel) is  $\sim 40\%$  at  $\Delta C = 0$ . The virial mass of A478 is more massive than the average of 50 clusters (Section 3) and our data is shallower than those of 50 clusters, but nonetheless the contamination is less than half of those of clusters  $z \sim 0.2$ .

There are two reasons for low contamination of the very nearby cluster ( $z \sim 0.09$ ). First, since the colors of red-sequence galaxies become more blue as the redshift decreases, the number of red background galaxies increases. Second, the ratio of member to background galaxies for very nearby clusters becomes lower because an apparent covering area becomes larger. Therefore, the dilution effect for clusters at lower redshifts becomes drastically less significant. It is consistent with the feature of the very nearby cluster of Hydra-A ( $z \sim 0.05$ ).



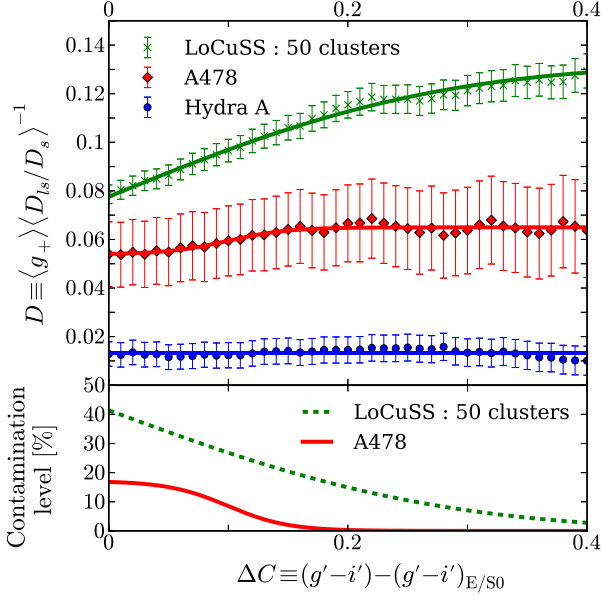


**Figure 2.** Top: dilution estimator,  $D = \langle g_+ \rangle / \langle D_{ls}/D_s \rangle$ , as a function of color offset from the cluster red sequence. The red diamonds, blue circles, and green crosses show  $D$  for A478, Hydra A, and an ensemble of 50 clusters from the LoCuSS project, respectively. The relative lensing strengths  $D$  for A478 and the LoCuSS 50 clusters increase with increasing  $\Delta C$ , while  $D$  for Hydra A is randomly distributed. The solid lines represent the best-fit models to describe the color distribution of member galaxies. Bottom: contamination level calculated by the respective best-fit model as a function color offset. The red-solid and green-dashed lines show the results of A478 and the LoCuSS 50 clusters, respectively.

In order to securely select background galaxies, we employ 1% contamination level following Okabe et al. (2013) and define background galaxies with  $\Delta C > 0.17$  for A478. As for Hydra A, we do not apply the color cut because of the tiny contamination level, because  $D$  is almost constant in the wide color range of  $-1 < \Delta C < 1$ . In order to assess our background selection for Hydra A, we make another background catalog selected with the same color cut of A478, conduct a weak lensing mass measurement (Section 3) and confirm the result dose not change. The background number densities for A478 and Hydra A are  $n_{\text{bkg}} = 6.2 [\text{arcmin}^{-2}]$  and  $28.9 [\text{arcmin}^{-2}]$ , respectively. The mean source redshifts for A478 and Hydra A are  $\langle z_s \rangle \simeq 0.643$  and  $\langle z_s \rangle \simeq 0.591$ , respectively.

### 3 MASS MEASUREMENTS

Tangential distortion signals contain full information on the lensing signals of clusters. Since clusters can be considered as gravitationally bound spherical objects at zeroth order, a measurement of tangential shear profile is a powerful way to measure cluster masses. The tangential shear is measurable by averaging over sufficient background galaxies, in order to suppress shape noise attributable to random intrinsic ellipticities of background galaxies. We measure a mean tangential shear  $\langle g_{+,i} \rangle$  as an average of the tangential shear component of background galaxies residing in the  $i$ -th radial

bin with the statistical weight of  $w_g$ . The other distortion component,  $g_{\times}$ , which is the 45 degree rotated component, is also estimated. Hereafter, we refer to  $\langle g_{+(\times),i} \rangle$  as  $g_{+(\times),i}$ .

In order to interpret the lensing signals, we here briefly introduce mass models as the cluster mass density profile. The reduced tangential shear profile for mass models can be expressed by

$$g_+(\theta) = \frac{\bar{\kappa}(<\theta) - \kappa(\theta)}{1 - \kappa(\theta)}, \quad (1)$$

where  $\bar{\kappa}$  and  $\kappa$  are the mean surface mass density within a radius  $\theta$  and the surface mass density at  $\theta$ , respectively. The lensing signals are computed by  $\bar{\kappa}$  and  $\kappa$  for given mass models.

The NFW model (Navarro, Frenk & White 1996, 1997) is a theoretically well-motivated mass model according to numerical simulations of dark matter particles. They found that the matter density profile of CDM halos is well described by an analytic function

$$\rho_{\text{NFW}}(r) = \frac{\rho_s}{(r/r_s)(1 + r/r_s)^2}, \quad (2)$$

where  $\rho_s$  is the central density parameter and  $r_s$  is the scale radius. The asymptotic mass density slopes are  $\rho \propto r^{-1}$  and  $r^{-3}$  for  $r \ll r_s$  and  $r \gg r_s$ , respectively. The NFW profile is specified by two parameters of  $M_\Delta$  which is a mass enclosed within a sphere of radius  $r_\Delta$ , and the halo concentration  $c_\Delta = r_\Delta/r_s$ . Here,  $r_\Delta$  is the radius inside of which the mean density is  $\Delta$  times the critical mass density,  $\rho_{\text{cr}}(z)$ , at the redshift,  $z$ . For a comparison, we model a singular isothermal sphere (SIS) profile for the main halo, given by

$$\rho_{\text{SIS}}(r) = \frac{\sigma_v^2}{2\pi G r^2}, \quad (3)$$

where  $\sigma_v^2$  is a one-dimensional velocity dispersion. We also consider the BCG mass model to estimate the lensing signals for the BCGs. Since the innermost radii for the profiles are outside the BCGs, the tangential shear from the BCGs is sensitive to the interior mass within  $\theta$ , in other words,  $\kappa(\theta) = 0$  in Equation (1). Since the internal structure for the BCGs cannot be resolved by lensing signals, we reasonably employ the point mass,  $M_{\text{pt}}$ , to estimate the BCG mass, in terms of  $g_+(\theta) \propto M_{\text{pt}}/(\pi\theta^2)$ .

Given specific mass models, we perform  $\chi^2$  fit to the tangential shear profile,  $g_+$ . The  $\chi^2$  is defined as followed:

$$\chi_g^2 = \sum_{i,j} (g_{+,i} - g_{+,i}^{\text{model}}) C_{ij}^{-1} (g_{+,j} - g_{+,j}^{\text{model}}), \quad (4)$$

where

$$C_{ij} = C_{\text{stat},ij} + C_{\text{LSS},ij}. \quad (5)$$

The first term of  $C$  is the statistical noise relevant to the intrinsic ellipticity of background galaxies. The statistical noise for the shear is given by  $C_{\text{stat},ij} = \bar{\sigma}_{g,i}^2 \delta_{ij}/2$ , where  $\bar{\sigma}_{g,i}$  is the statistical uncertainty of the two components in the  $i$ -th radial bin and  $\delta_{ij}$  is Kronecker's delta. The second term,  $C_{\text{LSS},ij}$ , is the error covariance matrix of uncorrelated large-scale structure (LSS) along the line-of-sight, (e.g. Schneider et al. 1998; Hoekstra 2003; Umetsu et al. 2011, 2014; Oguri et al. 2010; Oguri & Takada 2011; Okabe et al. 2013, 2014a), estimated from the weak-lensing power spectrum with WMAP7 cosmology (Komatsu et al. 2011). The

cosmic shear correlation function leads to non-zero off-diagonal elements for  $C_{\text{LSS},ij}$ .

The signal-to-noise ratio (S/N) for the tangential shear profile is computed by

$$\left(\frac{S}{N}\right)^2 = \sum_{ij} g_{+,i} C_{ij}^{-1} g_{+,j}. \quad (6)$$

### 3.1 A478

The tangential reduced-shear profile for A478 is shown in Figure 3, in a range of  $100 \text{ kpc} \lesssim r \lesssim 5.5 \text{ Mpc}$ . The innermost radius, determined by requiring a sufficient number of background galaxies, is larger than the effective radius of the BCG. The S/N of the tangential shear profile is 8.1. The tangential shear profile exhibits a clear curvature. On the other hand, the B-mode,  $g_{\times}$ , shows both negative and positive values, which is consistent with null signal. We plot  $\theta \cdot g_{\times}(\theta)$  in the bottom panel of Figure 4, so that the scatter is independent of radius for logarithmically spaced binning (Miyatake et al. 2013).

We fit a single NFW model or two components of the NFW model as the smooth matter density profile and the point source ( $g_{+} = g_{\text{NFW}} + g_{\text{pt}}$ ; NFW+point) to the tangential shear profile (Table 2). The minimum chi-square are  $\chi^2_{\text{min}}(\text{d.o.f}) = 2.18(7)$  and  $2.12(6)$  for the first and second model, respectively, where the degree of freedom is presented in the round bracket. Here, since errors are mainly attributable to the variance of intrinsic ellipticity,  $\langle \sigma_g^2 \rangle^{1/2} \sim 0.4$ , in addition to measurement errors,  $\chi^2_{\text{min}}$  becomes small. It shows that two models are acceptable as the cluster mass model. In order to estimate the validity of the additional point source, we calculated F test probability, 0.7, indicating that there is no strong reason to add the point source to describe the current data. The best-fit SIS profile ( $\sigma_v = 958.67^{+58.11}_{-62.96} \text{ km s}^{-1}$ ) is deviated from the curvature of the tangential shear profile, albeit still acceptable ( $\chi^2_{\text{min}}(\text{d.o.f}) = 9.13(8)$ ).

### 3.2 Hydra A

A large apparent size of Hydra A allows us to estimate the tangential shear profile in a wide radial range of  $30 \text{ kpc} \lesssim r \lesssim 3 \text{ Mpc}$ , as shown in Figure 4. In particular, lensing signals at  $r \lesssim 50 - 100 \text{ kpc}$  is detected solely by weak-lensing analysis. It is an advantage of weak-lensing study of very nearby clusters, because cluster central regions at higher redshifts are in the strong-lensing regime. For instance, an innermost radius of a stacked lensing profile for 50 clusters  $z \sim 0.2$  (Okabe et al. 2013) is  $70 h_{70}^{-1} \text{ kpc}$ . The tangential profile is highly detected at  $S/N = 7.0$ . The profile shows two characteristic features: a sharp decrease in the central region ( $r < 100 \text{ kpc}$ ) and a clear curvature in the range of  $100 \text{ kpc} \lesssim r \lesssim 3 \text{ Mpc}$ . The B-mode values,  $g_{\times}$ , are randomly distributed cross the null signal.

First, we fit the profile with the NFW model and obtain a high concentration parameter  $c_{\text{vir}} = 9.37^{+6.99}_{-3.94}$  with virial mass  $M_{\text{vir}} = 2.74^{+1.99}_{-1.21} \times 10^{14} M_{\odot}$ . The best-fit mass profile shows a clear curvature (Figure 4). However, we found that the best-fit model is lower than the observed lensing signals at  $r \lesssim 50 \text{ kpc}$  and  $r \gtrsim 2 \text{ Mpc}$ . It suggests that the virial mass is underestimated because the mass estimate is sensitive to

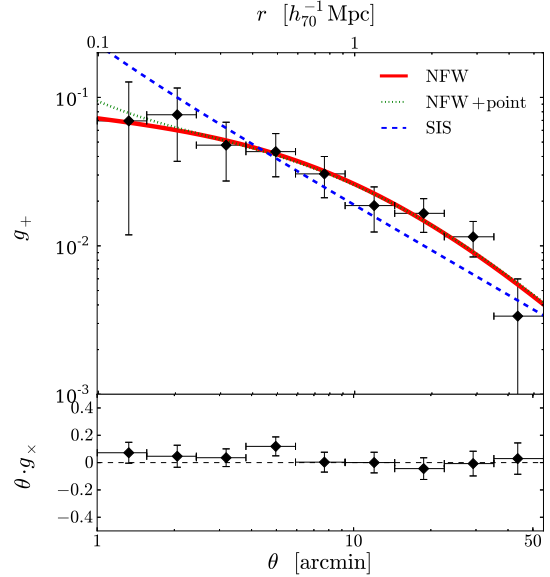


**Figure 3.** Radial profiles of the tangential reduced-shear component (top panel),  $g_{+}$ , and the  $45^{\circ}$ -rotated component (bottom panel),  $\theta \cdot g_{\times}$ , for A478. The vertical error bar of each data point ( $i$ -th bin) shows the diagonal element of the error covariance matrix,  $C_{ii}^{1/2}$  (Equation 5), for the top panel and  $\theta_i C_{ii}^{1/2}$  for the bottom panel, respectively. The tangential reduced-shear profile shows a clear radial curvature, in agreement with the steepening NFW profile. The red-solid, green-dotted, and blue-dashed lines show the best-fit NFW, NFW+point, and SIS profiles, respectively.

lensing signals in the outskirts. A similar deviation is found in the best-fit SIS model ( $\sigma_v = 631.93^{+43.71}_{-47.77} \text{ km s}^{-1}$ ). On the other hand, when we fit the NFW model to the lensing profile beyond  $150 \text{ kpc}$ , the best-fit concentration becomes lower  $c_{\text{vir}} = 4.52^{+2.95}_{-1.75}$  (Table 2). The best-fit profile well describes the data at  $r \gtrsim 300 \text{ kpc}$ , but significantly underestimates the signals at  $r \lesssim 100 \text{ kpc}$ .

It indicates that the inner slope of the tangential profile becomes steeper than expected from the outskirts. The steep inner slope suggests one possibility that an extra component exists inside the innermost radius. In particular, the slope for the lensing profile at a few inner bins is proportional to  $\sim -2$ . We thus consider two components of the NFW model and the point mass (NFW+point). The best-fit parameters are shown in Table 2. The  $\chi^2_{\text{min}}(\text{d.o.f})$  is improved from  $8.62(18)$  to  $4.02(17)$ . The best-fit profile well describes the data in the full radial range (Figures 4). In order to estimate the validity of the additional point source, we conducted F test and found that the probability  $4 \times 10^{-5}$  is significantly small. It is thus reasonable to add the extra component to the smooth mass component for describing the observed lensing signals. In other words, the two-components model better describes the tangential profile.

**Table 2.** Mass estimates for Hydra A and A478. The NFW mass ( $M_{\Delta}^{\text{NFW}}$ ) and the point mass ( $M_{\text{pt}}$ ) are in units of  $10^{14} h_{70}^{-1} M_{\odot}$  and  $10^{12} h_{70}^{-1} M_{\odot}$ , respectively.

Cluster	model & method	$M_{\text{vir}}^{\text{NFW}}$	$M_{200}^{\text{NFW}}$	$M_{500}^{\text{NFW}}$	$M_{1000}^{\text{NFW}}$	$M_{2500}^{\text{NFW}}$	$M_{\text{pt}}$
A478	NFW	$16.38^{+5.70}_{-4.41}$	$12.93^{+3.96}_{-3.22}$	$8.67^{+2.14}_{-1.88}$	$5.95^{+1.28}_{-1.17}$	$3.17^{+0.72}_{-0.72}$	—
A478	NFW+point	$16.72^{+6.30}_{-4.65}$	$13.05^{+4.12}_{-3.30}$	$8.56^{+2.19}_{-1.97}$	$5.74^{+1.55}_{-1.53}$	$2.93^{+1.28}_{-1.23}$	$< 25.90$
Hydra A	NFW ( $r > 150 h_{70}^{-1} \text{kpc}$ )	$4.66^{+2.77}_{-1.82}$	$3.62^{+1.85}_{-1.31}$	$2.40^{+0.95}_{-0.76}$	$1.63^{+0.55}_{-0.46}$	$0.85^{+0.29}_{-0.28}$	—
Hydra A	NFW+point (full radial range)	$4.88^{+3.29}_{-2.04}$	$3.66^{+2.05}_{-1.41}$	$2.27^{+0.98}_{-0.77}$	$1.43^{+0.55}_{-0.48}$	$0.64^{+0.32}_{-0.31}$	$6.10^{+2.47}_{-2.50}$

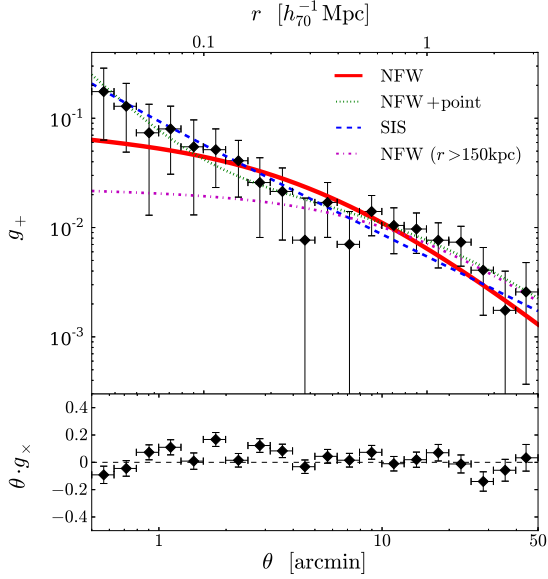


**Figure 4.** Radial profiles of the tangential reduced-shear component (top panel),  $g_+$ , and the  $45^\circ$ -rotated component (bottom panel),  $\theta \cdot g_x$ , for the Hydra A cluster, shown over a wide radial range of  $30 \text{kpc} \lesssim r \lesssim 3 \text{Mpc}$ . The red-solid, magenta-dot-dashed, green-dotted, and blue-dashed lines show the best-fit NFW profiles derived from the data at  $r > 30 \text{kpc}$  and  $r > 150 \text{kpc}$ , the best-fit NFW+point and SIS profiles, respectively.

## 4 JOINT ANALYSES

### 4.1 Joint Weak-lensing and Stellar Photometry Study of A478

We study the mass distribution of A478 using weak-lensing and BCG (PGC014685) photometry measurements.

The tangential shear profile (Section 3.1) for A478 is well described by a single NFW model or a two-component mass model including the BCG as an unresolved point mass. Complementary information at small scales is useful to directly determine the BCG mass profile as well as to better constrain the total mass profile in combination with lensing data.

For this purpose, we use stellar mass estimates of the BCG from a photometry. We estimate the stellar mass for the BCG using  $K$ -band photometry using the  $K$ -correction and galactic extinction from 2MASS extended source catalog (Skrutskie et al. 2006). Since the  $K$ -band luminosity is sensitive to the light of old stars and less sensitive to recent star-

formation activities, it serves as a reasonable proxy for stellar mass. The difference in  $K$ -band transmission between the 2MASS and traditional Johnson  $K$  filters is not important for our purpose (Carpenter 2001). We employ both empirical (Arnouts et al. 2007) and theoretical (Longhetti & Saracco 2009) scaling relations between the stellar mass and  $K$ -band luminosity. We consider the Salpeter (Salpeter 1955), Chabrier (Chabrier 2003) and Kroupa (Kroupa 2001) IMFs. The mass uncertainty is estimated by taking into account the photometric errors, 15% intrinsic scatter for the empirical scaling relation (Arnouts et al. 2007), and systematic uncertainties from different scaling relations.

We assume a pseudo isothermal mass distribution (PIEMD) model (Eliásdóttir et al. 2007; Limousin et al. 2009; Natarajan et al. 2009) to describe the stellar mass distribution of the BCG. The PIEMD model is specified with three parameters, namely, the core radius ( $a$ ), the scale radius ( $s$ ), and the normalization ( $\rho_0$ ), in the following form:

$$\rho = \frac{\rho_0}{(1 + r^2/a^2)(1 + r^2/s^2)} \quad (s \geq a). \quad (7)$$

The projected surface luminosity profile for the BCG is shown in Figure 5. The profile is fitted with the PIEMD model convoluted with the PSF kernel. We find that the outer edge of the luminosity profile is slightly truncated and deviated from expectations for the PIEMD model. Although the truncated PIEMD model would be better to fit the overall profile, the deviation is small for this study and thus we adopt the PIEMD model here. We obtain  $a = 2.7 \text{kpc}$  and  $s = 11.3 \text{kpc}$ . Assuming a scaling relation between cuspy radius and the luminosity for BCGs (Lauer et al. 2007), the mean core radius is expected to be  $a \sim 0.8 \text{kpc}$ . The best-fit core radius is larger than the mean one calculated from the scaling relation, which might be caused by a limitation of ground-based telescope because the apparent size of the expected core radius,  $\sim 0.5 \text{arcsec}$ , is small. We find the best-fit solution by minimizing the combined  $\chi^2$  function,  $\chi^2 = \chi_g^2 + \chi_s^2$ , with  $\chi_s^2$  defined by

$$\chi_s^2 = \frac{(M_* - M_{\text{PIEMD},*})^2}{\delta_{M_*}^2}. \quad (8)$$

Here,  $M_*$  and  $\delta_{M_*}$  are the stellar mass and its uncertainty estimated with specific IMFs within the measurement radius  $17 \text{kpc}$ , respectively.  $M_{\text{PIEMD}}$  is the model for the BCG. We determine the normalization of the PIEMD model and the NFW parameters from the joint fit.

Figure 6 shows the best-fit model for the tangential shear profile and the BCG stellar mass profile. The Chabrier and Kroupa IMFs give total stellar mass estimates of  $M_{\text{BCG},*}^{\text{Cha}} \sim M_{\text{BCG},*}^{\text{Kro}} \sim 8 \times 10^{11} M_{\odot}$ , compared to

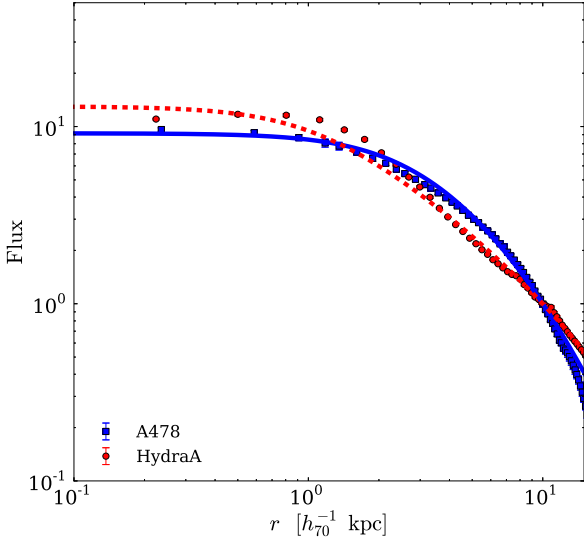


**Figure 5.** Projected surface luminosity profiles for BCGs in A478 (red circles) and the Hydra A cluster (blue squares) in arbitrary units. The solid and dotted lines denote the best-fit profiles for A478 and the Hydra A cluster, respectively

$M_{\text{BCG},*}^{\text{Sal}} = (15 \pm 2) \times 10^{11} M_{\odot}$  with the Salpeter IMF, where the errors mainly account for systematic uncertainties from different scaling relations. The IMF uncertainty gives rise to a systematic bias on stellar mass estimates, as pointed out by Oguri, Rusu & Falco (2014). Hence, independent constraints, such as from stellar kinematics (Newman et al. 2009, 2011, 2013) quasar microlensing (Oguri, Rusu & Falco 2014) observations, are needed to meaningfully break the IMF uncertainty (see Section 4.2). Despite the IMF uncertainty, the best-fit NFW mass model ( $M_{\text{vir}} = 16.48 \times 10^{14} M_{\odot}$  and  $c_{\text{vir}} = 4.56_{-1.28}^{+1.67}$ ) is not sensitive to the choice of IMF because the lensing signal from the main cluster halo is sufficiently high. We note that the result does not significantly change when we adopt  $a = 0.8 \text{ kpc}$ .

#### 4.2 Joint Weak-lensing and Stellar Kinematics Study of Hydra A

The tangential shear profile for the Hydra A cluster is well described by the two-component mass model of the BCG’s point mass and the smooth NFW profile (Section 3.2). The smooth mass component is determined by fitting lensing signals at outer cluster radii, whereas the point mass measurement is sensitive to lensing signals at innermost bins because the BCG lensing signal is embedded in the lensing signals of the main cluster. Recently Newman et al. (2009, 2011, 2013) performed a joint analysis of weak/strong-lensing and stellar kinematics data to break the IMF uncertainty and measure the mass profile from the BCG to the cluster main halo. They demonstrated that the BCG stellar kinematics is powerful for determining the BCG mass profile and the cluster inner mass profile under two assumptions of dynamic equilibrium and mass tracing light. Following their pioneering studies, we here conduct a joint weak-lensing and stellar-

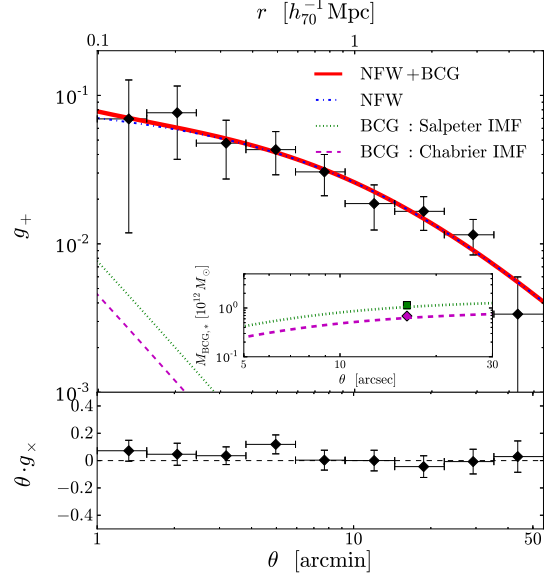


**Figure 6.** Tangential reduced-shear profile and BCG stellar mass profile (inset) for A478. The red-solid line represents the best-fit solution for the total lensing signal with the NFW (blue dot-dashed line) plus BCG (Salpeter IMF) model. The green-dotted and magenta-dashed lines show the best-fit lensing profiles and BCG stellar mass profiles, obtained with the Salpeter and Chabrier IMFs, respectively.

kinematics analysis of Hydra A. We note that there are no publicly available data of stellar kinematics for A478. Since the Hydra A cluster is at a very low redshift, strong-lensing information is not required for our joint analysis.

We here summarize the dynamical properties of the BCG (3C218). It is well known that the AGN in the BCG ejects a pair of jets, showing interaction between the jets and surrounding ICM (McNamara et al. 2000). Fujita et al. (2013) have discovered a dust lane in the central region of the BCG ( $4 \text{ kpc} \times 0.8 \text{ kpc}$ ). The major axis is along the east-west direction, nearly perpendicular to the jet axis. Hamer et al. (2014) found that the dust lane is a rotating disk by measuring several line emissions. The maximum rotating velocity reaches  $\sim 400 \text{ km s}^{-1}$ . Melnick, Gopal-Krishna & Terlevich (1997) also found a fast rotating disk using the H $\alpha$  line. Ekers & Simkin (1983) measured stellar velocities and pointed out that the BCG is composed of a rotating disk of stars embedded in non-rotating stellar components. The rotational velocity inside  $4''$  ( $\sim 4 \text{ kpc}$ ) is found to be  $\sim 50 \text{ km s}^{-1}$  (Loubser et al. 2008). The stellar velocity dispersion is  $\sim 200\text{--}300 \text{ km s}^{-1}$  (Heckman et al. 1985; Loubser et al. 2008). Therefore, the central part of the BCG ( $\lesssim 4''$ ) comprises cold rotating disk, rotating stellar, and non-rotating stellar components, exhibiting complex dynamics. On the other hand, the non-rotating stellar components dominate outside the rotating disk ( $\gtrsim 4''$ ).

We use the PIEMD model (Equation 7), assuming spherically symmetry, isotropic orbits, and mass tracing light. We determine the core and scale radii by fitting the light distribution (Figure 5) and then estimate the nor-



malization of the PIEMD and the NFW parameters by a joint fit to weak-lensing and stellar velocity dispersion measurements. The combined  $\chi^2$  function is defined by  $\chi^2 = \chi_g^2 + \chi_{\text{dyn}}^2$ , where

$$\chi_{\text{dyn}}^2 = \sum_i \frac{(\sigma_{v,*} - \sigma_{\text{l.o.s.}})^2}{\delta_{\sigma_{v,*}}^2} \quad (9)$$

with  $\sigma_{v,*}$  and  $\delta_{\sigma_{v,*}}$  the velocity dispersion and its uncertainty, respectively. The velocity dispersion along the line-of-sight,  $\sigma_{\text{l.o.s.}}$ , is computed by the spherical Jeans equation (eq. 42 of Cappellari 2008)

$$\Sigma_* \sigma_{\text{l.o.s.}}^2(R) = 2G \int_R^\infty \frac{\nu_*(r) M(r) F(r)}{r^{2-2\beta}} dr \quad (10)$$

(see also eq 12 of Newman et al. 2013), where  $M(r) = M_{\text{PIEMD},*}(r) + M_{\text{NFW}}(r)$  is the total mass,  $\beta = 1 - \sigma_\theta^2/\sigma_r^2$  presents the velocity anisotropy, and  $\nu_*$  and  $\Sigma_*$  are the spherical and surface density profiles of the stellar components, respectively; here we use the best-fit light distribution of the PIEMD model to describe  $\nu_*$  and  $\Sigma_*$ . The kernel  $F(r)$  is  $(r^2 - R^2)^{1/2}$  for the isotropic-orbit case,  $\beta = 0$  (see Cappellari 2008; Elíasdóttir et al. 2007). Lemze et al. (2012) studied the radial dependence of  $\beta(r)$  for simulated cluster-sized dark-matter halos, finding  $\beta \sim 0 - 0.2$  at  $\sim 0.05 r_{\text{vir}}$ . Since the line-of-sight integral is weighted by the stellar density and thus dominated by the innermost region, the results are insensitive to  $\beta(r)$  around the BCG. Hence, we can reasonably assume a constant  $\beta$ . We fix  $\beta = 0$  throughout the paper. We also checked that these results are not sensitive to the choice of  $\beta$  and do not change significantly when fitting with  $\beta = 0.2$ . We use the stellar velocity dispersion at  $r > 4''$  where the contribution from the non-rotating component is negligible. We summarize the lensing data, projected velocity dispersion and the light profile for the BCG in Table A1. The best-fit radial profiles of weak-lensing and projected velocity dispersion are shown in the left panel of Figure 7. The best-fit profile for the total lensing signal at  $r \lesssim 100$  kpc is systematically lower than the measurements, although consistent within errors.

The spherical mass profiles  $M(< r)$  in the central region ( $r < 300$  kpc) are shown in the right panel of Figure 7. The stellar mass component (green dotted line) dominates over the NFW halo component (blue dotted line) at  $r \lesssim 20$  kpc. The NFW mass component from the joint fit is consistent with the best-fit NFW profile from the  $g_+$  fitting using the data at  $r > 150$  kpc (yellow region). The total mass profile (black solid line) agrees with the weak-lensing-only results using the full-range data ( $r > 30$  kpc; cyan region) because these best-fit tangential profiles are similar at  $r \lesssim 100$  kpc (Figures 4 and 7). The NFW+point total mass profile from tangential-shear fitting (magenta region) is in good agreement at  $r \gtrsim 150$  kpc with that from the joint analysis, but overestimates the joint results at  $r \lesssim 50$  kpc. We shall discuss this point in the last paragraph of this section as well as in Section 4.3. We note that the best-fit BCG mass profile is extrapolated beyond the maximum radius for the light-profile measurements ( $\sim 30$  kpc) assuming a constant mass-to-light ratio. If the mass profile for the BCG is sharply truncated at this radius, the BCG mass is  $M_{\text{BCG}} = 1.0_{-0.4}^{+0.3} \times 10^{12} M_\odot$ .

For comparison, we overplot the dynamical masses es-

timated from the cold gas disk component (blue diamonds; Hamer et al. 2014) and hydrostatic masses from X-ray observations (David et al. 2001, red circles). A detailed comparison of weak-lensing and X-ray mass measurements at mass overdensities  $\Delta < 2500$  are presented in Okabe et al. (2014b). Hamer et al. (2014) assumed a rotating exponential disk for the central cold disk and obtained dynamical mass estimates within 3.2 kpc and 2.2 kpc using the H $\alpha$  and Pa $\alpha$  lines, respectively. David et al. (2001) derived hydrostatic mass estimates using *Chandra* data.

Overall, our results agree well with independent measurements from dynamical masses estimated from the cold gas disk and X-ray hydrostatic mass estimates, over a wide range of radii from a few kpc to 300 kpc, irrespective of different physical conditions and nature of cold gas particles, hot diffuse plasmas, and stars used as mass tracers. Although the effects of non-thermal pressure (e.g., sound waves, subsonic gas motions, and cosmic rays) are expected to be significant as triggered by AGN activities, the X-ray and weak-lensing mass measurements in the central region are in excellent agreement. Since turbulent and/or rotational gas motions in the ICM can be directly probed by the SXS onboard *Astro-H*, a complementary combination of kinetic information about the ICM, cold gas, and stars and weak-lensing data will be able to provide an improved understanding of the physical state of the cluster center.

We also estimate the stellar mass of the BCG using  $K$ -band luminosities as described in Section 4.1. An empirical scaling relation (Arnouts et al. 2007) gives  $M_{\text{BCG},*} \sim 5_{-1}^{+3} \times 10^{11} M_\odot$ , within a photometric aperture radius of 17 kpc. The errors represent a 15% scatter in the stellar mass-to-light ratio (Arnouts et al. 2007). The inferred stellar mass is in remarkable agreement with the BCG mass determined by our joint analysis (Figure 7). Using the theoretically-predicted scaling relation (Longhetti & Saracco 2009, Table 2), we find  $M_{\text{BCG},*} \sim 4 - 6 \times 10^{11} M_\odot$  for the Salpeter IMF. On the other hand, the Chabrier (Chabrier 2003) and Kroupa (Kroupa 2001) IMFs give a stellar mass of  $\sim 3 \times 10^{11} M_\odot$ , which is slightly lower than our best-fit estimate.

The best-fit tangential shear profile at  $r \lesssim 100$  kpc is somewhat discrepant with the data. Newman et al. (2009, 2013) took into account a calibration factor,  $m_{\text{WL}} = g_{+, \text{obs}}/g_{+, \text{true}}$ , for their lensing model (i.e.,  $g_{+, \text{model}} \rightarrow m_{\text{WL}} \times g_{+, \text{model}}$ ), possibly caused by systematic shear calibration and/or redshift errors, to solve the discrepancy between their lensing and dynamical data. Newman et al. (2009) found  $m_{\text{WL}} = 0.80$ , and Newman et al. (2013) used a prior  $m_{\text{WL}} = 0.89 \pm 0.05$ , meaning that their shear measurements are underestimated by  $\sim 10\%$ – $20\%$ , relative to their dynamical measurements.

We repeated fitting including an additional correction factor  $m_{\text{WL}}$  as a free parameter and obtained  $m_{\text{WL}} = 3.42 \pm 1.24$ , which is extremely higher than our shear calibration uncertainty ( $2 - 3\%$ ; Okabe et al. 2013, 2014a; Okabe & Smith 2015). It is therefore unlikely that the discrepancy is primarily caused by shear calibration errors, suggesting alternative possibilities, such as the choice of mass models. We estimate lensing signals from member galaxies located in the gap between the BCG-kinematics and weak-lensing data regions ( $8 \text{ kpc} \lesssim r \lesssim 30 \text{ kpc}$ ), assuming a stellar mass-to-light ratio based on the Salpeter IMF. Including

their contributions, the best-fit lensing profile is enhanced by  $\sim 20\%$ , which however is insufficient to account for the discrepancy. In the joint analysis, we assumed that the BCG stellar mass traces the light distribution, and did not explicitly include BCG's dark-matter contribution relative to the NFW form. If there is a significant and extended dark-matter contribution associated with the BCG, the apparent discrepancy may be explained. We shall examine this hypothesis in the next subsection.

#### 4.3 Additional Dark-Matter Component around the BCG in Hydra A

For the Hydra A cluster, the total mass profile around the BCG has been tightly constrained by the joint analysis of weak-lensing and dynamical data. We find that the inferred stellar mass contribution is not sufficient to fully explain the observed lensing signal  $g_+ \propto r^{-2}$  at  $r \sim 100$  kpc. This may imply that there is an additional dark-matter component associated with the BCG. Here, we adopt as a working hypothesis that the central dark-matter distribution  $\rho_{\text{DM}}(r)$  is shallower than that of the stellar component  $\rho_*(r)$ , namely  $\rho_{\text{DM}}(r) < \rho_*(r)$  at  $r \rightarrow 0$  and  $\rho_{\text{DM}}(r) > \rho_*(r)$  at larger radii. We have first attempted to fit with the generalized NFW model  $\rho \propto (r/r_s)^{-\gamma}(1+r/r_s)^{-3+\gamma}$  and the cored NFW model  $\rho \propto (1+r/r_c)^{-1}(1+r/r_s)^{-2}$ , both described by three parameters, to account for the hypothetical dark-matter contribution. We find both models fall short of the central tangential shear signal and fail to explain the discrepancy.

Now we employ the PIEMD model to describe the additional mass component around the BCG. We express the total mass in Equation (10) as  $M(r) = M_{\text{PIEMD},*}(r) + M_{\text{PIEMD},\text{DM}}(r) + M_{\text{NFW}}(r)$ , where  $M_{\text{PIEMD},\text{DM}}(r)$  is specified by three parameters, namely the normalization, core and scale radii. We here assume the minimum core radius to be  $0.4'$  in order to satisfy the requirement that the dark matter distribution is shallower than the stellar distribution, because there is no visible tracer of hypothetical dark-matter profile, that is, the current data is not sufficient to constrain the shape of the profile.

Figure 8 shows the resulting best-fit tangential shear profile  $g_+(\theta)$  (left) and the spherical mass profile  $M(< r)$  (right). We find that adding the extended central dark-matter component can fully account for the dynamical and lensing data. The change on the total mass profile due to the additional dark-matter component is small (right panel of Figure 8). The resulting total mass profile agrees better with those from independent measurements. In Figure 9 we show the spherical mass density profiles for the total, dark-matter, NFW and BCG stellar components in the central region. The dark-matter density profile at  $1 \text{ kpc} \lesssim r \lesssim 20 \text{ kpc}$  is shallower than the stellar density profile, as imposed by the prior (the bottom panel in Figure 9). The slope for the total matter density is perturbed by the BCG stellar and the additional dark-matter components from the slope of the NFW main halo. The minimized  $\chi^2_{\text{min}}(\text{d.o.f.}) = 6.1$  (20) has been improved from 9.0 (23) relative to the NFW model. The  $F$  test gives a probability of  $5 \times 10^{-2}$ , thus supporting the addition of the flat dark-matter component to explain better both lensing and kinematics data.

Lensing systematics, such as the effects of halo/BCG

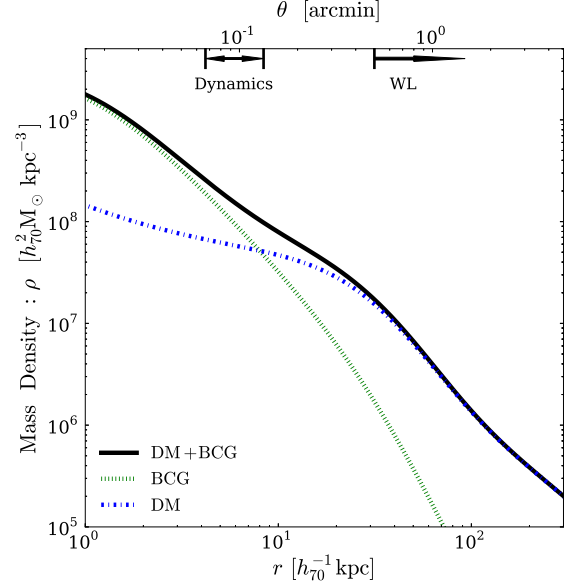


**Figure 9.** Top: mass density profiles in the central region of Hydra A. The black-solid, green-dashed, blue-dotted and red-dotted lines show the total, BCG stellar, dark-matter, and NFW mass density profiles, respectively. Bottom: mass density slope,  $-d \ln \rho / d \ln r$ . The best-fit dark-matter density profile is shallower than the stellar density profile at  $1 \text{ kpc} \lesssim r \lesssim 20 \text{ kpc}$ , as imposed by the prior and favored by the data.

triaxiality (e.g. Corless & King 2007; Oguri & Blandford 2009; Meneghetti et al. 2010; Umetsu et al. 2015a), cannot also be ignored as one of the possible causes of the discrepancy between weak-lensing data and the best-fit model for the NFW and BCG stellar mass components (Section 4.2). Since the additional dark-matter component would not be a unique solution to explain the discrepancy, it is also crucial to investigate other possibilities. Sophisticated model of the triaxial/rotational/non-axisymmetric halo model for stellar kinematics and weak-lensing data would be critically important for a deeper understanding of the connection between the BCGs and host dark matter halo. Further systematic studies of very nearby clusters are of vital importance for understanding of the mass distribution around BCGs.

#### 4.4 Dark-Matter Fraction around the BCG in Hydra A

Isobaric cooling time scales for the two clusters are less than 1 Gyr within the central 30 kpc (David et al. 2001; Sun et al. 2003). Gas cooling thus causes condensation of baryons, leading to formation of stars and contraction of dark matter in the central cluster region. One of the most plausible scenarios for the dark-matter response to the cooling of baryons is adiabatic contraction (e.g. Gnedin et al. 2004). A joint analysis of stellar kinematics ( $\lesssim 8 \text{ kpc}$ ) and weak lensing data ( $\gtrsim 30 \text{ kpc}$ ) for the Hydra A cluster allows us to decompose the observed total projected mass profile into the stellar and dark-matter components around the BCG, which provides us with a good opportunity to test the validity of adiabatic contraction models in the central region.

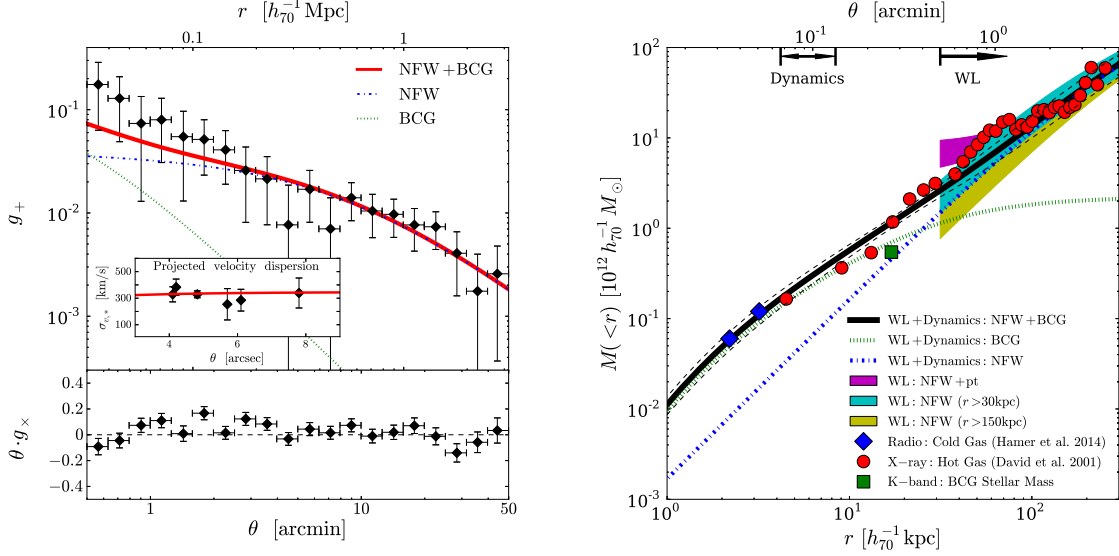


**Figure 7.** Left: tangential reduced-shear for the Hydra A cluster and projected velocity dispersion for the central BCG (inset). Circles and triangles denote Heckman et al. (1985) and Loubser et al. (2008) for projected velocity dispersion, respectively. The red-solid lines represent the best-fit models for the total lensing signal and the projected velocity dispersion. The dotted-green and blue-dot-dashed lines show the lensing signals for the BCG and NFW mass components, respectively. The back-solid and dashed-lines represent the total mass profile and its  $1\sigma$  uncertainty, respectively. The green-dotted and blue-dot-dashed lines represent the BCG stellar and NFW halo components, respectively. The magenta, cyan, and yellow shaded areas (from the top to the bottom) show the  $1\sigma$  error regions for the NFW+point, NFW ( $r > 30$  kpc), and NFW ( $r > 150$  kpc) models from the weak-lensing-only fits, respectively. The blue diamonds, red circles, and green squares show dynamical mass estimates from radio-line measurements of cold gas (Hamer et al. 2014), hydrostatic mass estimates from X-ray emitting hot gas (David et al. 2001), and stellar mass estimates from  $K$ -band photometry assuming the Salpeter IMF, respectively. The top arrows indicate the radial ranges for the dynamical data and weak-lensing data.

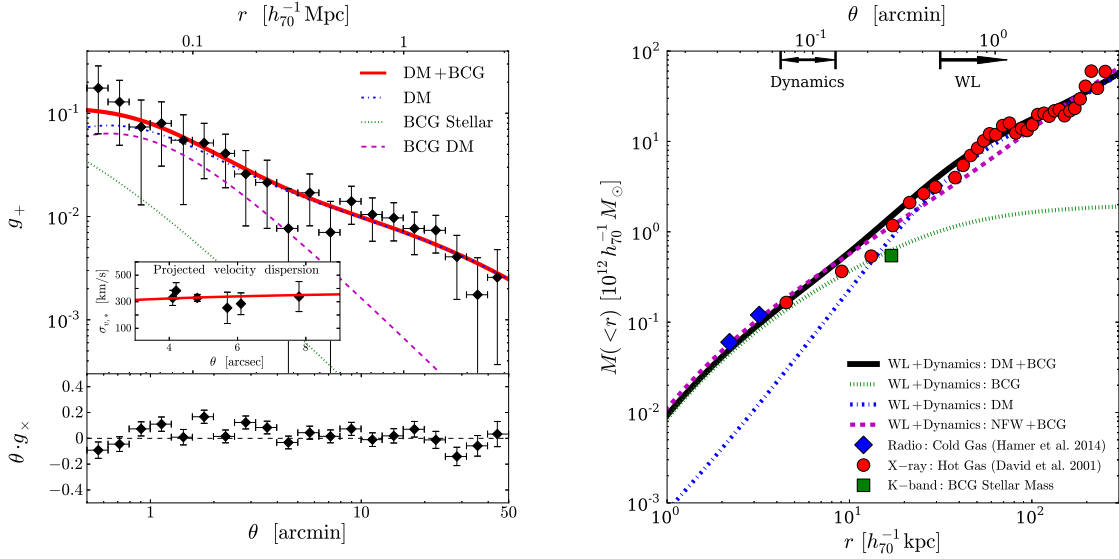


**Figure 8.** Left: results for Hydra A including an additional extended dark-matter component associated with the BCG. The red-solid lines show the best-fit models for the total lensing signal and the projected velocity dispersion. The green-dotted, magenta-dashed, and blue-dot-dashed lines are the lensing signals for the stellar component, the dark-matter component associated with the BCG, and the NFW halo component, respectively. Right: spherical mass profile within 300 kpc. The back-solid, green-dotted, and blue-dotted-dashed lines show the results for the total mass, stellar mass, and total dark-matter distributions, respectively. For comparison, the total mass profile in Figure 7 is shown by the magenta-dashed line. The blue diamonds, red circles, and green squares are the same as those in Figure 8.

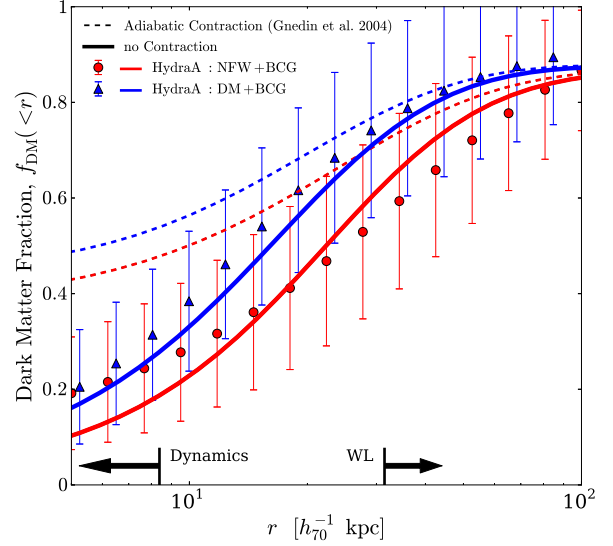
Here we estimate dark-matter mass fractions around the BCG, given by  $f_{\text{DM}} = M_{\text{DM}}/(M_{\text{DM}} + M_* + M_{\text{gas}})$ , where  $M_{\text{DM}}$  is the dark-matter mass,  $M_*$  is the stellar mass, and  $M_{\text{gas}}$  is the gas mass (David et al. 2001). We employ the NFW (Sections 4.1 and 4.2) and composite dark-matter (NFW+PIEMD; Section 4.3) models to calculate  $M_{\text{DM}}(< r)$ . The stellar mass is composed of the BCG and cluster elliptical galaxies. The BCG stellar mass profile is calculated using the best-fit parameters given in Section 4.2. The stellar masses for other elliptical member galaxies are estimated by their  $K$ -band luminosities. Here, we assume the Salpeter IMF (Section 4.2) because the stellar mass estimated by the Salpeter IMF agrees with that estimated by the stellar kinematics.

Figure 10 shows the resulting dark-matter fraction profiles for the Hydra A cluster. The cumulative dark-matter fractions progressively increase with increasing the cluster radius. The slope is slightly steeper beyond the effective radii of BCGs,  $r_e \sim 20$  kpc, and flattened at  $r \sim 100$  kpc. Similar results have been reported by earlier work (e.g. Nagino & Matsushita 2009; Oguri, Rusu & Falco 2014). Nagino & Matsushita (2009) found that the integrated mass-to-light ratio profiles for early-type galaxies based on the X-ray and photometry analysis increases beyond effective radii  $r_e$  of galaxies. Oguri, Rusu & Falco (2014) conducted a joint analysis of strong lensing and stellar photometry for a large ensemble of elliptical galaxies, finding that the slope of the dark-matter fraction becomes steeper at  $r > r_e$ .

Now we examine the dark-matter fractions using models with and without adiabatic contraction (Gnedin et al. 2004). We use the Jaffe model (Jaffe 1983) as a stellar mass distribution, where the density profile follows  $\rho(r) \propto r^{-2}(r+s)^{-2}$ . In the limit of  $r \gg a$  for the PIEMD model (Equation (7)), the PIEMD density profile resembles the Jaffe profile. For the dark-matter component, we only consider the NFW model. The dark-matter fractions (dashed lines) predicted by adiabatic contraction models (Gnedin et al. 2004) overestimate our measurements. On the other hand, models without adiabatic contraction agree better with the dark-matter fractions, consistent with the results of Newman et al. (2013) and Oguri, Rusu & Falco (2014). This suggests that other physical processes are critically important to suppress the modification of dark-matter profile.

## 5 DISCUSSION

We find that the adiabatic contraction model (Gnedin et al. 2004) overestimates the dark-matter fraction profiles compared to our measurements (Section 4.4). One of possible scenarios is that the gas outflows driven by AGN activities suppress condensation of the dark-matter distribution in the central region (e.g. Teyssier et al. 2011; Martizzi et al. 2012; Ragone-Figueroa, Granato & Abadi 2012). In fact, on-going jet activities of central AGNs have been reported in two clusters (David et al. 2001; Sun et al. 2003; Diehl et al. 2008, e.g.). The projected distances between the BCG and X-ray bubbles triggered by the observed activities are  $r \sim 25$  kpc for Hydra A and  $r \sim 9$  kpc for A478, respectively (e.g. David et al. 2001; Sun et al. 2003; Wise et al.



**Figure 10.** Dark-matter fractions as a function of spherical cluster radius. The red circles and blue triangles show the results for Hydra A using the best-fit NFW (Section 4.2) and NFW+PIEMD (Section 4.3) profiles, respectively. The solid and dashed lines are the dark-matter fractions predicted by models without and with adiabatic contraction, respectively (Gnedin et al. 2004). The two arrows mark the radial range which covers each data.

2007; Diehl et al. 2008). Three-dimensional characteristic scale radii obtained by equating the interior stellar and NFW masses are  $r_{\text{eq}} \sim 25$  kpc for Hydra A;  $r_{\text{eq}} \sim 22$  kpc and  $\sim 15$  kpc for A478, assuming the Salpeter and Chabrier IMFs, respectively. This suggests that the current AGN jet activities can directly affect the baryons over the region where stellar mass dominates. Although there is an uncertainty between the three-dimensional radius,  $r_{\text{eq}}$ , and the projected distances between the BCG and X-ray bubbles, the results hold even if the jet/bubble direction is  $\lesssim 40^\circ$  from the plane of the sky. Another alternative scenario assumes minor, dry (dissipationless) mergers of clumpy structures (e.g. El-Zant, Shlosman & Hoffman 2001; Lackner & Ostriker 2010), which can flatten the central dark-matter density profile (Section 4.3) and be closely correlated with the BCG growth.

Further systematic studies of central dark-matter mass fractions and density slopes, using a large sample of AGN and non-AGN clusters, are required to distinguish between the effects of gas outflows and dissipationless mergers, for deep understanding of physical processes governing the BCG growth. Systematic joint studies combining weak lensing and stellar kinematics data will also be useful to examine correlations between stellar population properties and IMF constraints inferred from joint analyses (McDermid et al. 2014).

## 6 SUMMARY

We have presented a weak-lensing study of the nearby cool-core clusters Hydra A and A478. To minimize dilution of



the lensing signal due to contamination by cluster members, we carefully select populations of background source galaxies in the color-magnitude plane. Compared to weak-lensing studies of clusters at intermediate redshifts  $z \sim 0.2$  (Okabe et al. 2013), the level of background contamination by cluster members is significantly reduced. This enables us to obtain a larger number of background galaxies for weak-lensing measurements while achieving a low level of contamination. This is one of the advantages of weak-lensing analysis of very nearby clusters.

The S/N ratios for detection of the tangential shear signals are 7.0 and 8.1 for Hydra A and A478, respectively, after accounting for the contribution from projected uncorrelated LSS. The resulting S/N ratios are comparable to those of clusters at  $z \sim 0.2$ , thanks to the increased number of background galaxies behind the clusters.

We find that the tangential shear profile for A478 is well fitted with a single NFW model. For Hydra A, the tangential shear signal in the central region is well described by a two-component model including the central BCG as an unresolved point mass.

We find that the choice of IMFs can introduce a large uncertainty (factor of  $\sim 2$ ) in the BCG stellar mass estimates, which makes it difficult to decompose the observed total projected mass profile into the stellar and dark-matter components (Section 4.1). On the other hand, as demonstrated by Newman et al. (2009, 2011, 2013), the internal stellar kinematics of BCGs enables us to precisely measure the mass profiles of two components independent of the IMF uncertainty (Section 4.2). For Hydra A, we find that the central mass profile ( $< 300$  kpc) determined from weak lensing is in excellent agreement with those from independent measurements, including dynamical masses estimated from the cold gas disk component, X-ray hydrostatic total mass estimates, and central stellar mass estimates. For the BCG, the data prefer the Salpeter IMF to the Chabrier and Kroupa IMFs. An additional flat dark-matter component around the BCG accounts simultaneously for the weak-lensing and stellar-kinematics data for Hydra A.

Dark-matter fractions around the BCGs for the Hydra A cluster are found to be smaller than those predicted by adiabatic contraction models, and to agree well with model predictions without contraction. This implies that other baryonic processes, such as the AGN feedback, dissipationless mergers, or the combination of the two, could play important roles in shaping the central cluster mass profile. A precise joint measurement of the central cluster mass profile provides us with complementary information about the dynamics of hot intracluster gas, which will be directly probed by Astro-H. Stellar kinematics data for the BCG of A478 is also important for future works.

## ACKNOWLEDGMENTS

We are grateful to N. Kaiser for developing the IMCAT package and making it publicly available. We thank Masamune Oguri, Masanori Nakamura, Takashi Hamana, Claire Nicole Lackner and Alexie Leauthaud for helpful discussions. This work was supported by “World Premier International Research Center Initiative (WPI Initiative)” and the Funds for the Development of Human Resources in Science and

Technology under MEXT, Japan, and Core Research for Energetic Universe in Hiroshima University (the MEXT program for promoting the enhancement of research universities, Japan). N.Okabe (26800097), M. Takizawa (26400218), and K. Sato (25800112) are supported by a Grant-in-Aid from the Ministry of Education, Culture, Sports, Science, and Technology of Japan. K. Umetsu acknowledges partial support from the Ministry of Science and Technology of Taiwan (grant MOST 103-2112-M-001-030-MY3).

## REFERENCES

- Anderson L. et al., 2014, MNRAS, 441, 24
- Arnouts S. et al., 2007, A&A, 476, 137
- Bertin E., Arnouts S., 1996, A&AS, 117, 393
- Blumenthal G. R., Faber S. M., Flores R., Primack J. R., 1986, ApJ, 301, 27
- Broadhurst T., Takada M., Umetsu K., Kong X., Arimoto N., Chiba M., Futamase T., 2005, ApJ, 619, L143
- Cappellari M., 2008, MNRAS, 390, 71
- Cappellari M. et al., 2006, MNRAS, 366, 1126
- Carpenter J. M., 2001, AJ, 121, 2851
- Chabrier G., 2003, PASP, 115, 763
- Corless V. L., King L. J., 2007, MNRAS, 380, 149
- David L. P., Nulsen P. E. J., McNamara B. R., Forman W., Jones C., Ponman T., Robertson B., Wise M., 2001, ApJ, 557, 546
- Diehl S., Li H., Fryer C. L., Rafferty D., 2008, ApJ, 687, 173
- Eggen O. J., Lynden-Bell D., Sandage A. R., 1962, ApJ, 136, 748
- Ekers R. D., Simkin S. M., 1983, ApJ, 265, 85
- El-Zant A., Shlosman I., Hoffman Y., 2001, ApJ, 560, 636
- Elíasdóttir Á. et al., 2007, ArXiv e-prints
- Fujita Y. et al., 2013, PASJ, 65, L15
- Gao L., Loeb A., Peebles P. J. E., White S. D. M., Jenkins A., 2004, ApJ, 614, 17
- Gao L., Navarro J. F., Frenk C. S., Jenkins A., Springel V., White S. D. M., 2012, MNRAS, 425, 2169
- Gnedin O. Y., Kravtsov A. V., Klypin A. A., Nagai D., 2004, ApJ, 616, 16
- Hamana T. et al., 2003, ApJ, 597, 98
- Hamer S. L. et al., 2014, MNRAS, 437, 862
- Heckman T. M., Illingworth G. D., Miley G. K., van Breugel W. J. M., 1985, ApJ, 299, 41
- Hinshaw G. et al., 2013, ApJS, 208, 19
- Hoekstra H., 2003, MNRAS, 339, 1155
- Hoekstra H., Franx M., Kuijken K., 2000, ApJ, 532, 88
- Ilbert O. et al., 2009, ApJ, 690, 1236
- Jaffe W., 1983, MNRAS, 202, 995
- Kaiser N., Squires G., Broadhurst T., 1995, ApJ, 449, 460
- Komatsu E. et al., 2011, ApJS, 192, 18
- Kroupa P., 2001, MNRAS, 322, 231
- Lackner C. N., Ostriker J. P., 2010, ApJ, 712, 88
- Lauer T. R. et al., 2007, ApJ, 662, 808
- Lemze D. et al., 2012, ApJ, 752, 141
- Limousin M., Sommer-Larsen J., Natarajan P., Milvang-Jensen B., 2009, ApJ, 696, 1771
- Longhetti M., Saracco P., 2009, MNRAS, 394, 774
- Loubser S. I., Sansom A. E., Sánchez-Blázquez P., Soechting I. K., Bromage G. E., 2008, MNRAS, 391, 1009

- Martizzi D., Teyssier R., Moore B., Wentz T., 2012, *MNRAS*, 422, 3081
- McDermid R. M. et al., 2014, *ApJ*, 792, L37
- McNamara B. R. et al., 2000, *ApJ*, 534, L135
- Melnick J., Gopal-Krishna, Terlevich R., 1997, *A&A*, 318, 337
- Meneghetti M., Rasia E., Merten J., Bellagamba F., Ettori S., Mazzotta P., Dolag K., Marri S., 2010, *A&A*, 514, A93
- Miyatake H. et al., 2013, *MNRAS*, 429, 3627
- Miyazaki S. et al., 2002, *PASJ*, 54, 833
- Mochizuki Y. et al., 2014, *ApJ*, submitted
- Nagino R., Matsushita K., 2009, *A&A*, 501, 157
- Natarajan P., Kneib J.-P., Smail I., Treu T., Ellis R., Moran S., Limousin M., Czoske O., 2009, *ApJ*, 693, 970
- Navarro J. F., Frenk C. S., White S. D. M., 1996, *ApJ*, 462, 563
- Navarro J. F., Frenk C. S., White S. D. M., 1997, *ApJ*, 490, 493
- Newman A. B., Treu T., Ellis R. S., Sand D. J., 2011, *ApJ*, 728, L39
- Newman A. B., Treu T., Ellis R. S., Sand D. J., Nipoti C., Richard J., Jullo E., 2013, *ApJ*, 765, 24
- Newman A. B., Treu T., Ellis R. S., Sand D. J., Richard J., Marshall P. J., Capak P., Miyazaki S., 2009, *ApJ*, 706, 1078
- Niikura H., Takada M., Okabe N., Martino R., Takahashi R., 2015, *PASJ*
- Oguri M., Bayliss M. B., Dahle H., Sharon K., Gladders M. D., Natarajan P., Hennawi J. F., Koester B. P., 2012, *MNRAS*, 420, 3213
- Oguri M., Blandford R. D., 2009, *MNRAS*, 392, 930
- Oguri M., Rusu C. E., Falco E. E., 2014, *MNRAS*, 439, 2494
- Oguri M., Takada M., 2011, *Phys. Rev. D*, 83, 023008
- Oguri M., Takada M., Okabe N., Smith G. P., 2010, *MNRAS*, 405, 2215
- Okabe N., Bourdin H., Mazzotta P., Maurogordato S., 2011, *ApJ*, 741, 116
- Okabe N., Futamase T., Kajisawa M., Kuroshima R., 2014a, *ApJ*, 784, 90
- Okabe N., Smith G. P., 2015, *ArXiv e-prints*
- Okabe N., Smith G. P., Umetsu K., Takada M., Futamase T., 2013, *ApJ*, 769, L35
- Okabe N., Takada M., Umetsu K., Futamase T., Smith G. P., 2010, *PASJ*, 62, 811
- Okabe N., Umetsu K., 2008, *PASJ*, 60, 345
- Okabe N. et al., 2014b, *PASJ*, 66, 99
- Ouchi M. et al., 2004, *ApJ*, 611, 685
- Percival W. J. et al., 2001, *MNRAS*, 327, 1297
- Planck Collaboration et al., 2013, *ArXiv e-prints*
- Ragone-Figueroa C., Granato G. L., Abadi M. G., 2012, *MNRAS*, 423, 3243
- Salpeter E. E., 1955, *ApJ*, 121, 161
- Sanderson A. J. R., Finoguenov A., Mohr J. J., 2005, *ApJ*, 630, 191
- Sato T. et al., 2012, *PASJ*, 64, 95
- Schneider P., van Waerbeke L., Jain B., Kruse G., 1998, *MNRAS*, 296, 873
- Skrutskie M. F. et al., 2006, *AJ*, 131, 1163
- Sun M., Jones C., Murray S. S., Allen S. W., Fabian A. C., Edge A. C., 2003, *ApJ*, 587, 619
- Teyssier R., Moore B., Martizzi D., Dubois Y., Mayer L., 2011, *MNRAS*, 414, 195
- Umetsu K., Broadhurst T., 2008, *ApJ*, 684, 177
- Umetsu K., Broadhurst T., Zitrin A., Medezinski E., Coe D., Postman M., 2011, *ApJ*, 738, 41
- Umetsu K., Medezinski E., Broadhurst T., Zitrin A., Okabe N., Hsieh B.-C., Molnar S. M., 2010, *ApJ*, 714, 1470
- Umetsu K. et al., 2014, *ApJ*, 795, 163
- Umetsu K. et al., 2015a, *ArXiv e-prints*
- Umetsu K., Zitrin A., Gruen D., Merten J., Donahue M., Postman M., 2015b, *ArXiv e-prints*
- Wise M. W., McNamara B. R., Nulsen P. E. J., Houck J. C., David L. P., 2007, *ApJ*, 659, 1153
- Yagi M., Kashikawa N., Sekiguchi M., Doi M., Yasuda N., Shimasaku K., Okamura S., 2002, *AJ*, 123, 66

## APPENDIX A: MULTIWAVELENGTH DATA OF THE HYDRA A CLUSTER

We here summarize the observing data and their measurement errors for the tangential shear profile, the projected velocity dispersion and the light profile for Hydra A.

This paper has been typeset from a  $\text{\LaTeX}$  file prepared by the author.

**Table A1.** Tangential shear ( $g_+$ ), projected velocity dispersion ( $\sigma_{v,*}$ ) and the core (a) and scale radii (s) of the PIEMD for the Hydra A. Note that the measurement error for the tangential shear ( $C = C_{\text{stat}} + C_{\text{LSS}}$ ) is weakly correlated. <sup>†</sup>:Heckman et al. (1985).<sup>‡</sup>:Loubser et al. (2008).

$\theta$ (arcmin)	$g_+$	$C^{1/2}$
$5.65922 \times 10^{-1}$	$1.75256 \times 10^{-1}$	$1.12041 \times 10^{-1}$
$7.13965 \times 10^{-1}$	$1.28711 \times 10^{-1}$	$7.97313 \times 10^{-2}$
$9.03514 \times 10^{-1}$	$7.36090 \times 10^{-2}$	$6.06401 \times 10^{-2}$
1.12847	$7.98743 \times 10^{-2}$	$4.91149 \times 10^{-2}$
1.43289	$5.48124 \times 10^{-2}$	$4.17630 \times 10^{-2}$
1.79821	$5.15705 \times 10^{-2}$	$2.83264 \times 10^{-2}$
2.27188	$4.08415 \times 10^{-2}$	$2.18615 \times 10^{-2}$
2.83350	$2.58124 \times 10^{-2}$	$1.76992 \times 10^{-2}$
3.57655	$2.13949 \times 10^{-2}$	$1.37130 \times 10^{-2}$
4.51228	$7.67107 \times 10^{-3}$	$1.09288 \times 10^{-2}$
5.69914	$1.69769 \times 10^{-2}$	$8.85021 \times 10^{-3}$
7.14476	$7.01793 \times 10^{-3}$	$7.00017 \times 10^{-3}$
8.97936	$1.40250 \times 10^{-2}$	$5.61649 \times 10^{-3}$
$1.12947 \times 10$	$1.04568 \times 10^{-2}$	$4.69525 \times 10^{-3}$
$1.42627 \times 10$	$9.69863 \times 10^{-3}$	$3.89583 \times 10^{-3}$
$1.78611 \times 10$	$7.65808 \times 10^{-3}$	$3.38880 \times 10^{-3}$
$2.25777 \times 10$	$7.34974 \times 10^{-3}$	$2.91867 \times 10^{-3}$
$2.84133 \times 10$	$4.07282 \times 10^{-3}$	$2.49727 \times 10^{-3}$
$3.56222 \times 10$	$1.74820 \times 10^{-3}$	$2.24314 \times 10^{-3}$
$4.41888 \times 10$	$2.57557 \times 10^{-3}$	$2.20707 \times 10^{-3}$
$\theta$ (arcmin)	$\sigma_{v,*}$ (kms <sup>-1</sup> )	$\delta\sigma_{v,*}$ (kms <sup>-1</sup> )
$6.83333 \times 10^{-2\dagger}$	$3.29000 \times 10^2$	$5.70000 \times 10$
$7.00000 \times 10^{-2\dagger}$	$3.83000 \times 10^2$	$6.10000 \times 10$
$8.03333 \times 10^{-2\dagger}$	$3.29000 \times 10^2$	$2.60000 \times 10$
$9.50000 \times 10^{-2\dagger}$	$2.54000 \times 10^2$	$1.18000 \times 10^2$
$1.01667 \times 10^{-1\dagger}$	$2.85000 \times 10^2$	$8.20000 \times 10$
$1.30000 \times 10^{-1\dagger}$	$3.39000 \times 10^2$	$1.13000 \times 10^2$
$a$ (arcmin)	$s$ (arcmin)	
$1.751265 \times 10^{-2}$	$4.68178 \times 10^{-1}$	